# Crystallographic spin torque conductivity tensor of epitaxial $IrO_2$ thin films for oxide spintronics

Michael Patton[1], Daniel A. Pharis[3], Gautam Gurung[9,10], Xiaoxi Huang[3], Gahee Noh[5], Evgeny Y. Tsymbal[4], Si-Young Choi[5,6,7], Daniel C. Ralph[3,8], Mark S. Rzchowski[2], Chang-Beom Eom[1*]

[1]Department of Materials Science and Engineering, University of Wisconsin-Madison, Madison, Wisconsin 53706, United States.

[2]Department of Physics, University of Wisconsin-Madison, Madison, Wisconsin 53706, United States.

[3]Cornell University, Ithaca, New York 14853, United States.

[4]Department of Physics and Astronomy & Nebraska Center for Materials and Nanoscience, University of Nebraska, Lincoln, NE 68588, United States.

[5]Department of Materials Science and Engineering, Pohang University of Science and Technology, Pohang, Gyeongbuk 37673, Korea.

[6]Center for Van der Waals Quantum Solids, Institute for Basic Science (IBS), Pohang 37673, Republic of Korea

[7]Semiconductor Engineering, Pohang University of Science and Technology (POSTECH), Pohang, 37673, Republic of Korea

[8]Kavli Institute at Cornell for Nanoscale Science, Ithaca, New York 14853, United States.

[9]Clarendon Laboratory, Department of Physics, University of Oxford, Parks Road, Oxford, OX1 3PU UK

[10]Trinity College, University of Oxford, Oxford, OX1 3BH UK

*Corresponding author: Chang-Beom Eom

Email: eom@engr.wisc.edu

## Abstract

Unconventional spin-orbit torques arising from electric-field-generated spin currents in anisotropic materials have promising potential for spintronic applications, including for perpendicular magnetic switching in high-density memory applications. Here we determine all the independent elements of the spin torque conductivity tensor allowed by bulk crystal symmetries for the tetragonal conductor $IrO_2$, via measurements of conventional (in plane) anti-damping torques for $IrO_2$ thin films in the high-symmetry (001) and (100) orientations. We then test that rotational transformations of this same tensor can predict both the conventional and unconventional anti-damping torques for $IrO_2$ thin films in the lower-symmetry (101), (110), and (111) orientations, finding good agreement. The results confirm that spin-orbit torques from all these orientations are consistent with the bulk symmetries of $IrO_2$, and show how simple measurements of conventional torques from high-symmetry orientations of anisotropic thin films can provide an accurate prediction of the unconventional torques from lower-symmetry orientations.

## Introduction

The linear-response spin current generated by an applied electric field within a material is described by a third-rank spin Hall conductivity (SHC) tensor $\sigma_{ij}^{s}$, where *s* is the index for the spin polarization direction, *i* for the spin flow direction, and *j* for the applied electric field direction. If the spin current is absorbed by an adjacent magnetic layer, it will apply a torque that can efficiently reorient the magnetization. The 27 elements within $\sigma_{ij}^{s}$ are often highly constrained by symmetry, and in commonly-used high-symmetry materials most of the elements are zero because symmetries can require the spin polarization, spin flow, and electric field to be mutually orthogonal[1]. We will term the torques generated by such a spin current as "conventional". For some applications, however, unconventional spin torques are highly desired. In particular, out-of-plane anti-damping torques associated with tensor elements of the form $\sigma_{zj}^{z}$ (where *z* is the direction normal to the device plane) are needed to drive efficient anti-damping switching of magnetic memory devices with perpendicular magnetic anisotropy. Such out-of-plane anti-damping torques have been realized using spin-source materials in which the symmetry constraints are relaxed by very low crystal symmetries or magnetic ordering[2–13] or by interfacial effects[14–16]. We have also recently proposed a simple alternative strategy for generating out-of-plane anti-damping torques -- to use a relatively high-symmetry but anisotropic material as the spin source (e.g., a tetragonal or orthorhombic structure) and to grow thin films with a growth axis tilted away from any high symmetry direction (e.g., tilted in a (101) or (111) orientation). In this case, the tilt of the crystal axes relative to the sample plane can break the necessary symmetries to allow a nonzero value for $\sigma_{zj}^{z}$ and an associated unconventional torque. We demonstrated this qualitatively in ref. [13] for the tetragonal material $IrO_2$. Here we test this approach quantitatively. By measuring the electric-field generated spin torque for (001) and (100) thin films of $IrO_2$ we determine all of the independent elements of the spin torque conductivity tensor associated with the absorbed spin current, and then we test whether rotational transformations of this single tensor can provide consistent quantitative predictions for the torques in three lower-symmetry film orientations: (110), (101), and (111). We find excellent agreement between the measurements and the predictions of the rotated tensor for both conventional and unconventional torques in all 5 crystal orientations.

## Results and Discussion

First, one note regarding notation. The electric-field-generated torque applied to the magnetic layer in a spin-source/magnet bilayer will differ from the spin current generated in the spin-source layer by an interfacial transmission coefficient which describes what fraction of the spin current is absorbed by the magnetic layer. Spin-torque experiments therefore do not measure the spin current directly. However, if the interfacial transmission coefficient is to a good approximation a constant ($T < 1$) that does not depend on the thin-film orientation or the spin orientation, the spin torque conductivity (STC) tensor as simply proportional to the bulk spin Hall conductivity tensor: $\tau_{ij}^{s} = T\sigma_{ij}^{s}$. Our analysis is not reliant on this assumption, however, and in fact one can view the purpose of the paper as being in part to test this assumption, i.e., to test the degree to which rotational transformations of a single STC tensor can give an accurate description of the measured torques for different crystal orientations.

The bulk crystal symmetries for the tetragonal structure of rutile $IrO_2$ dictate that the spin Hall conductivity tensor can be defined in terms of three independent elements. For the corresponding STC tensor we will call these elements *a*, *b*, and *c*. If we define basis vectors in terms of the $IrO_2$ crystal axes as X = [100], Y = [010], and Z = [001], the most general form allowed for the STC tensor is

$$\tau^{\boldsymbol{X}} \qquad\qquad \tau^{\boldsymbol{Y}} \qquad\qquad \tau^{\boldsymbol{Z}}$$

$$\begin{bmatrix} 0 & 0 & 0 \\ 0 & 0 & b \\ 0 & -a & 0 \end{bmatrix} \qquad \begin{bmatrix} 0 & 0 & -b \\ 0 & 0 & 0 \\ a & 0 & 0 \end{bmatrix} \qquad \begin{bmatrix} 0 & c & 0 \\ -c & 0 & 0 \\ 0 & 0 & 0 \end{bmatrix}.$$

Examples of spin currents corresponding to purely the *a*, *b*, and *c* processes are depicted in Fig. 1c. If a thin film of $IrO_2$ is grown in an orientation different than (001), one can perform a change of basis in order to define the STC tensor relative to basis vectors in the plane and perpendicular to the thin film. This is achieved through a rotational transformation of the form:

$$\tau_{ij}^{s} = \sum_{l,m,n} R_{il} R_{mj} R_{sn}\, \tau_{lm}^{n} \tag{1}$$

where $R_{il}$ are the elements of the appropriate rotation matrix. For example, for a (100) oriented $IrO_2$ film, using the basis vectors X = $[010]$, Y = [001], Z = [100], the STC tensor takes the form

$$\tau^{\boldsymbol{X}} \qquad\qquad \tau^{\boldsymbol{Y}} \qquad\qquad \tau^{\boldsymbol{Z}}$$

$$\begin{bmatrix} 0 & 0 & 0 \\ 0 & 0 & a \\ 0 & -b & 0 \end{bmatrix} \qquad \begin{bmatrix} 0 & 0 & -c \\ 0 & 0 & 0 \\ c & 0 & 0 \end{bmatrix} \qquad \begin{bmatrix} 0 & b & 0 \\ -a & 0 & 0 \\ 0 & 0 & 0 \end{bmatrix}.$$

The transformed forms of the STC tensor appropriate for the (101), (110), and (111) thin-film orientations of $IrO_2$ are listed in the supplemental information.

To determine the full STC tensor in $IrO_2$, the three elements *a, b,* and *c* must be experimentally measured. Spin-torque measurements in spin-source/magnet bilayer samples are only sensitive to spin currents flowing perpendicular to the sample plane, because only for this flow direction can the spin current be transmitted to the magnetic layer to exert a torque. This means that only the elements in the bottom rows (i.e., $\sigma_{Zj}^{s}$) of the STC tensor are accessible. The first element, $a$, can be measured using the (001)-orientated film, where an electric field is applied along the [010] direction resulting in a $[\bar{1}00]$-polarized spin current flowing in the out-of-plane [001] direction as indicated in Fig. 1b. The second element, *b*, can be measured using the (100) orientation, with an electric field applied along the in-plane [001] direction resulting in a $[0\bar{1}0]$-polarized spin current flowing in the out-of-plane [100] direction seen in Fig. 1e. The third and last term, *c*, can also be measured in the (100) orientation. An electric field applied along the [010] direction results in a $[001]$-polarized spin current flowing in the out-of-plane [100] direction seen in Fig. 1g.

To measure the electric-field-generated torques experimentally, high crystalline thin films of $IrO_2$ were grown via RF magnetron sputtering on different orientations of $TiO_2$ substrates, then capped *in situ* with ferromagnetic permalloy (Py), and patterned into device structures using the same methods described in our previous report[13]. High resolution x-ray diffraction (HRXRD) demonstrated a single high crystalline phase for all five thin-film $IrO_2$ orientations studied in this paper: (001), (100), (110), (101), and (111) (see Fig. 2a-e), and scanning transmission electron microscopy (STEM) also demonstrated sharp $IrO_2$/Py interfaces using STEM as shown in Fig. 2f-i. The spin-torque ferromagnetic resonance (ST-FMR) technique was used to characterize the SHC components by measuring ST-FMR resonance spectra as a function of sweeping the magnetic-field magnitude for a series of different directions of the magnetic-field within the plane of the sample. (See Methods for more details.)

The symmetric and antisymmetric ST-FMR amplitudes for the (001) and (100) orientations are shown in Fig. 1a,d, and f as a function of the angle of an in-plane applied magnetic field. The symmetric signals allow us to determine the three independent elements that define the anti-damping STC tensor of $IrO_2$ (see Methods). The first term *a*, determined in the (001) orientation, has a value of 520 ± 19 ($\frac{\hbar}{e}$ $(\Omega\ \mathrm{cm})^{-1}$). The second term *b*, determined in the (100) orientation with an electric field applied along the [001] direction, has a value of 238 ± 5 ($\frac{\hbar}{e}$ $(\Omega\ \mathrm{cm})^{-1}$). The third term *c* determined in the (100) orientation with electric field along the [010] direction, has a value of 493 ± 15 ($\frac{\hbar}{e}$ $(\Omega\ \mathrm{cm})^{-1}$). As required by symmetry for the (001) and (100) orientations with these electric-field directions (i.e., (001) with any in-plane E-field direction and (100) with E along [001] or [010]), we detect no unconventional torque components.

To test whether this same tensor gives a quantitative description of both the conventional and unconventional torques for other thin-film orientations, we also performed ST-FMR measurements for (110), (101), and (111) $IrO_2$ thin films. For each thin-film orientation, the measurements were made using various directions ($\psi$) of in-plane electric field (and hence charge current), with $\psi$ measured relative to the direction defined as the X axis for that orientation. For convenience in distinguishing the conventional and unconventional torques, we will plot the measured torque tensor components using a different set of coordinate axes (using lower-case x, y, and z), in which the x axis is along the applied electric field direction and z remains normal to the sample plane. The anti-damping torque components we measure for each orientation are then the conventional in-plane torque perpendicular to *E* (the tensor component $\tau_{zx}^{y}$), the unconventional in-plane torque parallel to E ($\tau_{zx}^{x}$), and the unconventional out-of-plane torque ($\tau_{zx}^{z}$). The results are shown as the symbols within the Fig. 3 graphs. The solid lines in Fig. 3 are the predicted STC values from the rotated experimental tensor, using the values of *a*, *b*, and *c* as determined above with no adjustable fit parameters. We find that, by using the STC tensor elements from the experimental (001) and (100) ST-FMR results and assuming the torque is governed by the bulk symmetries of $IrO_2$, the tensor rotation gives a good description of both the conventional and unconventional torque components for the other orientations. (Supplemental Note 3 shows zoomed-in plots of the unconventional torques.) For the (100), (110), (101), and (111) orientations, an unconventional in-plane STC was observed and followed the expected sin(2$\psi$) angular dependence, with a magnitude within 30 ($\frac{\hbar}{e}$ $(\Omega\ \mathrm{cm})^{-1}$) of the value predicted by the tensor rotation.. For the (101) and (111) orientations, unconventional out-of-plane anti-damping torque was also present, following an expected sin($\psi$) dependence, with a magnitude within 10 ($\frac{\hbar}{e}$ $(\Omega\ \mathrm{cm})^{-1}$) compared to the expectation from the tensor rotation. Both types of unconventional torques are significantly weaker than the conventional in-plane anti-damping torques, but this is fully consistent with the tensor rotation given the measured values of *a*, *b*, and *c*. For example, in the (111) orientation, the largest amplitude predicted by the tensor rotation for the out-of-plane anti-damping torque is predicted to be $(a-c)/2$ = 14 ± 24 ($\frac{\hbar}{e}$ $(\Omega\ \mathrm{cm})^{-1}$) (see supplemental information), or less than 3% of the conventional torque for the (001) orientation.

For the conventional in-plane anti-damping torque, the tensor rotation correctly predicts the observed dependence on the electric-field angle, but the magnitudes in some cases show somewhat larger deviations than for the unconventional torques. For example, the predicted conventional in-plane torque for the (111) orientation is about 20% lower than the measurements. One possible explanation for this could be due to the surface quality of the (001) and (100) orientations compared to (111). Due to the low surface energy of the (111) orientation, the interface between $IrO_2$ and Py is much sharper compared to the (001) and (100) orientations which could change the spin transparency at the interface. Compared to previous measurements for $IrO_2$ (001) and (110) grown by reactive oxide molecular beam epitaxy, the torque magnitudes for our (110) samples are in close agreement, whereas the torques for (001) orientation in our films are about a factor of two smaller.[17] This difference could be due to an Ir spacer layer included in the previous work or due to different growth techniques. The results in Fig. 3 correspond to anti-damping torque components. In addition, unconventional field-like torques were present in the (100), (110), (101), and (111) orientations which we attribute to anisotropic resistances within these orientations (see Fig. S9 in Supplemental Note 3)[5,18].

Despite the consistency of the experimentally-determined anti-damping spin-torque tensor for different crystal orientations, the experimental results are inconsistent with density-functional-theory (DFT) calculations of the spin Hall conductivity. The DFT predictions for the elements of the spin Hall conductivity tensor corresponding to the *a*, *b*, *c* parameters of the STC tensor are $a_{SHC}$= 254 ($\frac{\hbar}{e}$ $(\Omega\ \mathrm{cm})^{-1}$), $b_{SHC}$= 162 ($\frac{\hbar}{e}$ $(\Omega\ \mathrm{cm})^{-1}$), and $c_{SHC}$= 18 ($\frac{\hbar}{e}$ $(\Omega\ \mathrm{cm})^{-1}$). Despite the fact that the SHC magnitudes should be larger than the STC magnitudes on account of the interfacial spin transmission factor ($T < 1$), the spin Hall conductivities predict values that are too small, by more than a factor of 2 for the *a* parameter and by a factor of 27 for the *c* parameter. This leads to the measured conventional spin-orbit torques being significantly larger than expected from the DFT predictions. In contrast, the measured unconventional out-of-plane torque for low-symmetry crystal orientations is nevertheless much smaller than predicted by DFT. This is because the out-of-plane anti-damping torque is proportional to $a - c$, and this difference is much smaller for the torque parameters than the difference predicted by DFT, $a_{SHC} - c_{SHC}$. The poor agreement between measurements of spin-orbit torque and DFT predictions is true not only for $IrO_2$, but also for most materials including the prototypical spin source Pt [19,20]. This indicates that essential physics is still missing from this comparison. Nevertheless, since our tensor-rotation analysis depends only on the bulk symmetries of $IrO_2$ with no assumptions about microscopic mechanisms, predictions based on the rotated-tensor analysis remain valid and accurate.

A possible explanation of this behavior is the polycrystallinity of our Py films. This may cause diffuse scattering at the interface which is largely independent of the IrO2 crystal facet. It would be interesting to explore material systems where the ferromagnetic thin film is epitaxially grown on crystalline IrO2 or other spin-current source material to measure spin torques. In this case, the symmetry of the whole bilayer structure would control the spin torque, and the effect of interface breaking symmetry of the bulk spin-current source material could be elucidated. We leave these studies for future research.

## Conclusion

We have experimentally determined the full anti-damping spin torque conductivity tensor for $IrO_2$, and showed that this single tensor provides consistent and accurate results of the measured electric-field-driven torques for five different thin-film orientations, including both conventional and unconventional torques. The good agreement between the experimental measurements of the anti-damping spin torques and the predictions from the tensor rotation in Fig. 3 confirm that the electric-field-induced torques generated by $IrO_2$ originate from bulk spin currents within the $IrO_2$, with perhaps a minor contribution to the conventional spin torque in the (111) orientation from an additional interfacial effect. We observe no indication of large differences in interfacial spin transmission for different crystal orientations that would invalidate the tensor analysis. A possible explanation of this behavior is the polycrystallinity of our Py films, which causes diffuse scattering at the interface that is largely independent of the $IrO_2$ crystal facet. In addition, the tensor analysis show that it is possible to fully characterize the spin-torque tensor of an anisotropic material using measurements of conventional spin-orbit torque for selected high-symmetry crystal orientations, and then to obtain accurate predictions of the unconventional torques for lower-symmetry crystal orientations by means of a simple tensor rotation.

## Materials and Methods

*Sample growth, fabrication, and characterization.*

Epitaxial $IrO_2$ was grown on $TiO_2$ (001), (100), (110), (101) and (111) substrates by RF magnetron sputtering followed by *in situ* growth of ferromagnetic permalloy $Ni_{81}Fe_{19}$ (Py). The $IrO_2$ films were grown at 400°C at a pressure of 30 mTorr with 10% oxygen partial pressure. The target power was 20 W. After growth the sample was cooled in an $O_2$ atmosphere. Py was then grown in situ at room temperature, 4 mTorr of Ar, power of 35W, and a background pressure of 3E-7 Torr. The samples were then fabricated using photolithography and ion beam milling, followed by sputter deposition of 100 nm Pt/10nm Ti and lift off techniques for the electrodes.

*ST-FMR measurements*

During the ST-FMR measurements, a microwave current was applied at a fixed frequency (5-12 GHz) and fixed power (10-13 dBm) while sweeping an in-plane magnetic field through the Py resonance conditions from 0 to 0.15 T. The microwave current was modulated at a fixed frequency of 437 Hz and the mixing voltage across the device was measured using a lock-in amplifier. The mixing voltage was fitted vs applied field to extract the symmetric and antisymmetric Lorentzian components. For the angular-dependent ST-FMR, the applied field was rotated in-plane 360° and the symmetric and antisymmetric components were plotted as a function of angle. The out-of-plane ($T_{\perp}$) and the in-plane ($T_{\parallel}$) torques are proportional to the mixing voltage $V_{mix}$ as the ferromagnetic layer goes through its resonance condition, which can be fitted as a sum of a symmetric and an antisymmetric Lorentzians:

$$V_{mix,S} = -\frac{I_{rf}}{2}\left(\frac{dR}{d\varphi}\right)\frac{1}{\alpha(2\mu_0 H_{FMR}+\mu_0 M_{eff})}T_{\parallel}$$

$$V_{mix,A} = -\frac{I_{rf}}{2}\left(\frac{dR}{d\varphi}\right)\frac{\sqrt{1+M_{eff}/H_{FMR}}}{\alpha(2\mu_0 H_{FMR}+\mu_0 M_{eff})}T_{\perp} .$$

Here $I_{rf}$ is the RF current calibrated using Joule heating experiments, $R$ is the resistance of the device, $\varphi$ is the magnetization angle with respect to the applied current, $\alpha$ is the Gilbert damping coefficient determined from the ST-FMR linewidth (giving values in the range $\alpha$ = 0.013 - 0.037, $\mu_0 H_{FMR}$ is the resonance field, and $\mu_0 M_{eff}$ is the effective magnetization ranging from 0.6 - 0.85 T. The effective magnetization of Py is be obtained using Kittel's equation $f = \frac{\gamma}{2\pi}\sqrt{(H_{FMR}+H_K)(H_{FMR}+H_K+M_{eff})}$ where $\gamma$ is the gyromagnetic ratio and $H_K$ is the in-plane anisotropy field. Unconventional torques are characterized based on the dependence of the measured torques on the angle $\varphi$ of the magnetic field:

$$\mathrm{T}_{\parallel} = \mathrm{T}_{x,AD}\sin(\varphi) + \mathrm{T}_{y,AD}\cos(\varphi) + \mathrm{T}_{z,FL}$$

$$\mathrm{T}_{\perp} = \mathrm{T}_{x,FL}\sin(\varphi) + \mathrm{T}_{y,FL}\cos(\varphi) + \mathrm{T}_{z,AD}$$

$V_{mix,S}$ and $V_{mix,A}$ can then be expressed in the form of $\sin(2\varphi)(\mathrm{T}_{x,AD}\sin(\varphi) + \mathrm{T}_{y,AD}\cos(\varphi) + \mathrm{T}_{z,FL})$ and $\sin(2\varphi)(\mathrm{T}_{x,FL}\sin(\varphi) + \mathrm{T}_{y,FL}\cos(\varphi) + \mathrm{T}_{z,AD})$, respectively. Here the subscript x denotes a component associated with the spin polarization direction aligned with the applied electric field, and z the component associated with spin polarization normal to the sample plane. Additionally, here capital T represents the torque on the magnetic moment which is different than lowercase τ used denote the spin torque conductivity in the main text. The spin torque conductivity $\tau_{jk}^{i}$ can then be determined using $\tau_{jk}^{i} = \frac{\theta_i}{\rho_{IrO2}}\frac{\hbar}{2e}$, where $\rho_{IrO2}$ is the resistivity and $\theta_i$ is defined as:

$$\theta_i = \mathrm{T}_{i,AD}\frac{2e\mu_0 M_s t_{FM}}{\gamma\hbar J}$$

where $t_{FM}$ is the thickness of the ferromagnetic layer (Py or Ni) and *J* is the charge current density in the $IrO_2$. The resistivities were determined using Van der Pauw measurements and found to be 105 $\mu\Omega cm$ for (001), 226 $\mu\Omega cm$ for (100) along the [010] direction, 160 $\mu\Omega cm$ for (100) along the [001] direction, 100 $\mu\Omega cm$ for (101) along the [010] direction, 150 $\mu\Omega cm$ for (101) along the [10-1] direction, 95 $\mu\Omega cm$ for (111) along the [11-2] direction, and 105 $\mu\Omega cm$ for (111) along the [1-10] direction.

*Theoretical Calculations*

DFT calculations were performed using a Quantum-ESPRESSO code[21]. The plane-wave pseudopotential method with the fully relativistic ultrasoft pseudopotentials[22] was employed in the calculations. The exchange and correlation effects were treated within the generalized gradient approximation (GGA)[23]. The plane-wave cut-off energy of 40 Ry and a 16 × 16 × 16 k-point mesh in the irreducible Brillouin zone were used in the calculations. Spin-orbit coupling was included in all the calculations.

The spin Hall effect is given by:

$$\sigma_{ij}^{k} = \frac{e^2}{\hbar}\int \frac{d^3\vec{k}}{(2\pi)^3}\sum_{n} f_{n\vec{k}}\Omega_{n,ij}^{k}(\vec{k}),$$

$$\Omega_{n,ij}^{k}(\vec{k}) = -2Im\sum_{n\neq n'}\frac{\langle n\vec{k}|J_i^k|n'\vec{k}\rangle\langle n'\vec{k}|v_j|n\vec{k}\rangle}{\left(E_{n\vec{k}} - E_{n'\vec{k}}\right)^2} \quad ,$$

where $f_{n\vec{k}}$ is the Fermi-Dirac distribution for the *n*th band, $J_i^k = \frac{1}{2}\{v_i, s_k\}$ is the spin current operator with spin operator $s_k$, $v_j = \frac{1}{\hbar}\frac{\partial H}{\partial k_j}$ is the velocity operator, and $i, j, k = x, y, z$. $\Omega_{n,ij}^k(\vec{k})$ is referred to as the spin Berry curvature in analogy to the ordinary Berry curvature. In order to calculate the spin Hall conductivities, we construct the tight-binding Hamiltonians using PAOFLOW code[24,25] based on the projection of the pseudo-atomic orbitals (PAO) from the non-self-consistent calculations with a 16 × 16 × 16 *k*-point mesh. The spin Hall conductivities were calculated using the tight-binding Hamiltonians with a 48 × 48 × 48 *k*-point mesh by the adaptive broadening method to get the converged values.

**Acknowledgments**

CBE acknowledges support for this research through a Vannevar Bush Faculty Fellowship (ONR N00014-20-1-2844), the Gordon and Betty Moore Foundation's EPiQS Initiative, Grant GBMF9065. Transport measurement at the University of Wisconsin–Madison was supported by the US Department of Energy (DOE), Office of Science, Office of Basic Energy Sciences (BES), under award number DE-FG02-06ER46327. The authors gratefully acknowledge partial support of this research by NSF through the University of Wisconsin Materials Research Science and Engineering Center (DMR-2309000). Measurements at Cornell were supported by the DOE under award number DE-SC0017671. The work at UNL was partly supported by the National Science Foundation through the EPSCoR RII Track-1 program (Grant OIA-2044049). STEM measurement at Pohang University of Science and Technology was supported by the Basic Science Research Program through the National Research Foundation of Korea (NRF) funded by the Ministry of Science and ICT (2020R1A6C101A202).

**Author Contributions:**

M.P., D.R., and C.B.E. conceived the project. M.P. carried out the thin film growth, device fabrication, and spintronic measurements. D.P. and X.H. carried out additional device fabrication and supporting spintronic measurements. G.N. carried out the STEM experiments. G.G. performed theoretical calculations. C.B.E., M.S.R., D.C.R., S.Y.C., and E.Y.T. supervised the study. All authors discussed the results and commented on the manuscript. C.B.E. directed the research.

**Competing Interest Statement:**

The authors declare no conflict of interest.

## References


1. Seemann, M., Ködderitzsch, D., Wimmer, S. & Ebert, H. Symmetry-imposed shape of linear response tensors. *Phys Rev B Condens Matter Mater Phys* **92**, (2015).

2. Fukami, S., Anekawa, T., Zhang, C. & Ohno, H. A spin-orbit torque switching scheme with collinear magnetic easy axis and current configuration. *NATURE NANOTECHNOLOGY |* **11**, (2016).

3. Humphries, A. M. *et al.* Observation of spin-orbit effects with spin rotation symmetry. *Nat Commun* **8**, 911 (2017).

4. MacNeill, D. *et al.* Control of spin–orbit torques through crystal symmetry in WTe2/ferromagnet bilayers. *Nat Phys* **13**, 300–305 (2017).

5. Stiehl, G. M. *et al.* Current-Induced Torques with Dresselhaus Symmetry Due to Resistance Anisotropy in 2D Materials. *ACS Nano* **13**, 2599−2605 (2019).

6. Liu, Y. *et al.* Current-induced Out-of-plane Spin Accumulation on the (001) Surface of the IrMn 3 Antiferromagnet. *Phys Rev Appl* **12**, 64046 (2019).

7. Nan, T. *et al.* Controlling spin current polarization through non-collinear antiferromagnetism. *Nat Commun* **11**, 4671 (2020).

8. Zhao, B. *et al.* Unconventional Charge–Spin Conversion in Weyl-Semimetal WTe2. *Advanced Materials* **32**, 2000818 (2020).

9. Liu, L. *et al.* Symmetry-dependent field-free switching of perpendicular magnetization. *Nat Nanotechnol* **16**, 277–282 (2021).

10. You, Y. *et al.* Cluster magnetic octupole induced out-of-plane spin polarization in antiperovskite antiferromagnet. *Nat Commun* **12**, 6524 (2021).

11. Bai, H. *et al.* Control of spin-orbit torques through magnetic symmetry in differently oriented noncollinear antiferromagnetic Mn3Pt. *Phys Rev B* **104**, 104401 (2021).

12. Bose, A. *et al.* Tilted spin current generated by the collinear antiferromagnet ruthenium dioxide. *Nat Electron* **5**, 267–274 (2022).

13. Patton, M. *et al.* Symmetry Control of Unconventional Spin–Orbit Torques in IrO2. *Advanced Materials* **35**, (2023).

14. Baek, S.-H. C. *et al.* Spin currents and spin-orbit torques in ferromagnetic trilayers. *Nat Mater* **17**, 509–513 (2018).

15. Stiehl, G. M. *et al.* Layer-dependent spin-orbit torques generated by the centrosymmetric transition metal dichalcogenide β-MoTe2. *Phys Rev B* **100**, 184402 (2019).

16. Zhao, T. *et al.* Enhancement of Out-of-Plane Spin–Orbit Torque by Interfacial Modification. *Advanced Materials* **35**, (2023).

17. Bose, A. *et al.* Effects of Anisotropic Strain on Spin-Orbit Torque Produced by the Dirac Nodal Line Semimetal IrO2. *ACS Appl Mater Interfaces* **12**, 55411–55416 (2020).

18. Guimarã, M. H. D., Stiehl, G. M., Macneill, D., Reynolds, N. D. & Ralph, D. C. Spin−Orbit Torques in NbSe2/Permalloy Bilayers. *Nano Lett* **18**, 1311−1316 (2018).

19. Kontani, H., Naito, M., Hirashima, D. S., Yamada, K. & Inoue, J. Study of intrinsic spin and orbital Hall effects in Pt based on a (6s, 6p, 5d) tight-binding model. (2007) doi:10.1143/JPSJ.76.103702.

20. Zhu, L., Ralph, D. C. & Buhrman, R. A. Spin-Orbit Torques in Heavy-Metal-Ferromagnet Bilayers with Varying Strengths of Interfacial Spin-Orbit Coupling. *Phys Rev Lett* **122**, (2019).

21. Browning, R. *et al.* QUANTUM ESPRESSO: a modular and open-source software project for quantum simulations of materials. *J. Phys.: Condens. Matter* **21**, 395502 (2009).

22. Vanderbilt, D. Soft self-consistent pseudopotentials in a generalized eigenvalue formalism. *Phys Rev B* **41**, 7892–7895 (1990).

23. Perdew, J. P., Burke, K. & Ernzerhof, M. Generalized Gradient Approximation Made Simple. *Phys Rev Lett* **77**, 3865–3868 (1996).

24. Agapito, L. A., Ferretti, A., Calzolari, A., Curtarolo, S. & Nardelli, M. B. Effective and accurate representation of extended Bloch states on finite Hilbert spaces. *Phys Rev B* **88**, 165127 (2013).

25. Agapito, L. A., Ismail-Beigi, S., Curtarolo, S., Fornari, M. & Buongiorno Nardelli, M. Accurate tight-binding Hamiltonian matrices from ab initio calculations: Minimal basis sets. *Phys Rev B* **93**, 35104 (2016).

**Figures and Tables**

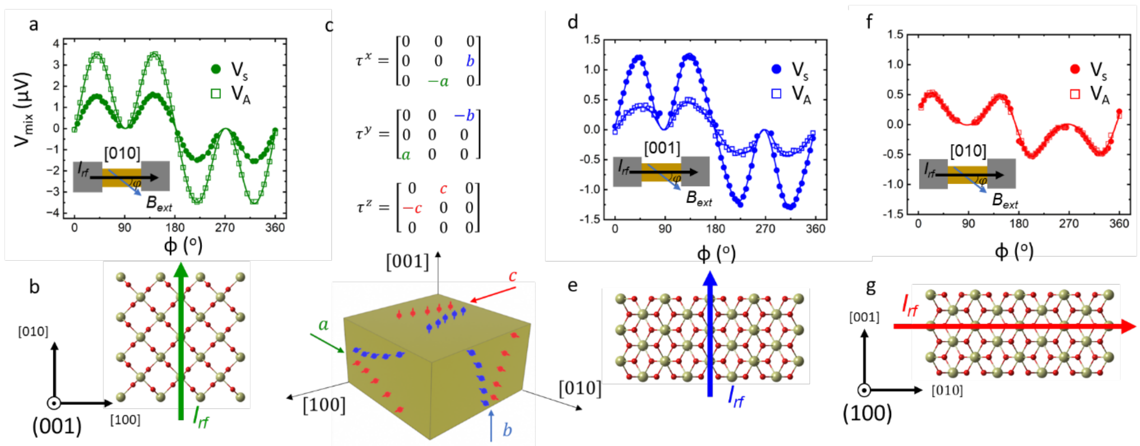


**Figure 1.** a, Symmetric and antisymmetric ST-FMR amplitudes as a function of magnetic-field angle for the (001) orientation with charge current along the [010] direction as depicted in b. c, experimental determination of the 3 non-zero STC elements using the (001) and (100) orientations. d, ST-FMR amplitudes as a function of magnetic-field angle for the (100) orientation with charge current along the [001] direction, as depicted in e. f, ST-FMR amplitudes as a function of magnetic-field angle for the (100) orientation with charge current along the [010] direction, as depicted in g.

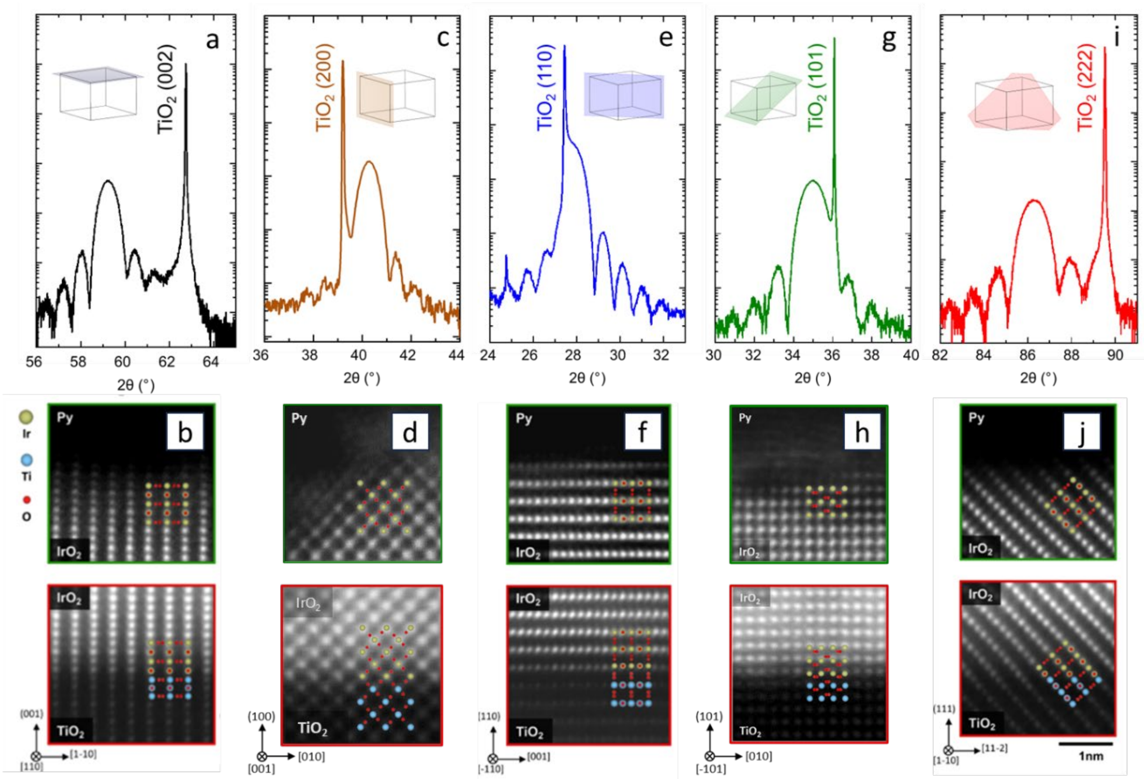


**Figure 2.** a, HR-XRD of the out of plane (002) peak and b, STEM of the interface between $IrO_2$ and Py and $TiO_2$ and $IrO_2$ with [1-10] zone axis. c, HR-XRD of the out of plane (200) peak and d, STEM of the interface between IrO2 and Py and $TiO_2$ and $IrO_2$ with [010] zone axis. e, HR-XRD of the out of plane (110) peak and f, STEM of the interface between $IrO_2$ and Py and $TiO_2$ and $IrO_2$ with [001] zone axis. g, HR-XRD of the out of plane (101) peak and h, STEM of the interface between $IrO_2$ and Py and $TiO_2$ and $IrO_2$ with [010] zone axis. And i, HR-XRD of the out of plane (222) peak and j, STEM of the interface between $IrO_2$ and Py and $TiO_2$ and $IrO_2$ with [11-2] zone axis.

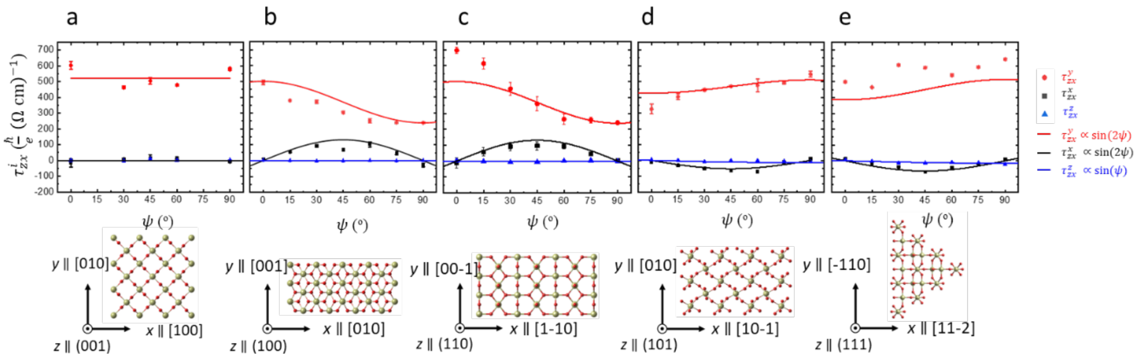


**Figure 3**: a-e, (001), (100), (110), (101), and (111) conventional and unconventional spin torque conductivities as a function of the angle $\psi$ of the in-plane electric field with respect to the x axis shown for each projection. Solid lines represent predictions based on rotating the experimental STC tensor, using the tensor elements determined from the ST-FMR results in the (001) and (100) orientations and the bulk symmetries of $IrO_2$.